# BIM-Integrated UAV Workflow for Automatic Facade Temperature Field Reconstruction Using IR Imagery and Component-Level Thermal Analysis

**Enrique Aldao[1], Gálata Martínez-Alonso[1], Gabriel Fontenla-Carrera[1], Higinio González-Jorge[1]**

[1]Aerolab, Instituto de Física Computatión e Ciencias Aeroespaciais (IFCAE), Universidade de Vigo, Ourense, 32004, Galicia, Spain

enrique.aldao.pensado@uvigo.gal, galata.martinez@uvigo.gal gabriel.fontenla@uvigo.gal higiniog@uvigo.gal

**Abstract -**

**Infrared thermography is a widely adopted non-destructive technique for infrastructure inspection, enabling the detection of defects such as thermal bridges, insulation deficiencies, moisture accumulation, and material degradation. In recent years, the use of this technique alongside Unmanned Aerial Vehicles (UAVs) has attracted growing interest due to their ability to access hard-to-reach areas such as facades and bridges. This work presents an automatised workflow for the efficient acquisition of facade temperature fields using UAVs. RGB imagery is employed to perform Structure-from-Motion and camera pose estimation, which is then used to reconstruct radiance fields of the facade surface. Radiometric calibration is performed using reference temperature probes, allowing the reconstruction of absolute temperature fields from raw infrared imagery. The proposed method enables the direct integration of calibrated thermal fields into Building Information Models (BIM), providing per-component thermal information for detailed inspection and data analysis. A practical case study on a multi-material facade demonstrates the workflow, highlighting its potential to enhance preventive maintenance and support energy-efficiency evaluations.**

**Keywords -**

**IR Imagery; Perspective-n-Point (PnP); Building Information Model (BIM); Unmanned Aerial Vehicle (UAV)**

## 1 Introduction

Infrared thermography has become a widely used non-destructive technique for the condition assessment of building facades, as it enables the detection of surface-temperature anomalies without physical contact [1, 2]. By measuring the spatial distribution of thermal radiation emitted by facade materials, the method can reveal a wide range of defects that may go unnoticed during visual inspections, including thermal bridges, insulation deficiencies, moisture accumulation, air leakage, and areas of material degradation [3, 4]. These anomalies are closely related to energy efficiency and structural integrity, making thermal imaging an effective tool for the preventive maintenance of built infrastructure [5].

Traditionally, facade inspections have been carried out by trained personnel using cranes, scaffolding, or specialised elevated platforms to access different areas of the structure and collect imagery. However, these methods are not only costly and time-consuming but also expose workers to significant risks associated with working at height [6]. To overcome these limitations, the use of Unmanned Aerial Vehicles (UAVs) has increased significantly in recent years. These platforms can be equipped with infrared cameras and complementary sensors, enabling the rapid, and efficient acquisition of data in hard-to-reach locations [7, 8, 9]. Furthermore, through the use of photogrammetric techniques, UAV imagery can be processed to generate high-resolution orthomosaics and detailed 3D reconstructions, thereby facilitating the integration of thermal and visual data within Building Information Models (BIM).

Although photogrammetry is well established for visual imagery, its direct application to infrared data remains challenging due to the lower spatial resolution of thermal cameras and the difficulty of identifying Ground Control Points (GCPs) in thermal images [10, 11]. To address this issue, several studies employ targets made of materials with contrasting emissivity or reflectivity as GCPs, which are easily detectable in infrared imagery. These targets are typically combined with high-accuracy positioning systems such as RTK-GNSS or terrestrial laser scanning to obtain precise reference coordinates [12]. While effective, this approach can be impractical for facade inspection because placing and surveying the targets at significant heights is often difficult and unsafe.

Conversely, other methods reconstruct the scene by combining RGB and infrared imagery. The RGB images are used to detect reference features such as corners or edges, which are then associated with their corresponding 3D coordinates [13, 14]. A Perspective-n-Point (PnP) approach is employed to estimate the camera poses, and the known relative transformation between the RGB and infrared cameras is used to project thermal textures onto the 3D model. Commercial software packages such as Agisoft Metashape and Pix4Dmapper currently support this workflow [15, 16]. However, their integration with BIM environments remains limited. Although they produce 3D reconstructions with mapped thermal textures, these results do not allow for the direct analysis of individual facade components. In addition, the thermal textures correspond to raw radiance values measured by the sensor, which require radiometric calibration to recover the actual temperature field. In light of these limitations, this work presents an IR inspection pipeline for reconstructing facade temperature fields using UAVs. The main contributions are as follows:

1. **Radiometric calibration:** Using a temperature probe and a set of radiometric control points, the proposed method reconstructs absolute temperature fields from raw infrared imagery.

2. **Direct integration with BIM:** The workflow enables the direct incorporation of calibrated temperature fields into BIM models, providing per-component thermal information that facilitates detailed inspection and data analysis.

The remainder of this article is structured as follows. Section 2 outlines the methodology used to reconstruct the facade temperature field, Section 3 presents and analyses the results, and Section 4 summarises the main findings.

## 2 Methodology

Figure 1 presents the workflow diagram of this work. First, experimental data are acquired, including UAV imagery, ground control point (GCP) data, and thermal reference point data of the building facade (Section 2.1). Next, this information is processed to perform structure-from-motion reconstruction and compute all camera poses (Section 2.2). Finally, the thermal field is calculated and integrated into the BIM reference frame (Section 2.3).


Figure 1. Thermal field reconstruction workflow.

### 2.1 Experimental data acquisition

As a practical case study, the facade shown in Figure 2 is selected for the IR inspection. It is a flat wall with different surface finishes and materials, as well as windows and a roof with varying reflectivity properties, which makes it particularly suitable for IR inspections. The facility is located in Ourense and belongs to Misturas SA, a company with which the University of Vigo collaborates through the RADIANCE project to develop intelligent robotic solutions in construction.

Figure 2. Facade chosen for the study.

To relate the camera poses to the BIM model, the positions of the Ground Control Points (GCPs) were first surveyed using a Leica DISTO X6 laser rangefinder [17] mounted on a Leica DST 360-X station. The DST 360-X includes a calibrated inclinometer and a horizontal encoder, allowing the direct measurement of 3D points with centimetre-level accuracy. Using this setup, the 3D coordinates of all window corners were recorded, providing a total of 20 GCPs distributed across the facade surface.

For the RGB and thermal data acquisition procedure, a UAV-based approach was chosen for practicality given the height of the building, for which a DJI Matrice 300 was employed. This UAV is equipped with a Zenmuse H20T hybrid camera system, which enables the synchronised acquisition of both RGB and infrared (IR) imagery. Table 1 summarises the main specifications of this imaging system. As shown, the visible-light sensor provides substantially higher resolution and a wider field of view, which facilitates the identification of GCPs and improves the accuracy of the camera pose estimation.

Table 1. Zenmuse H20T hybrid camera specifications according to the manufacturer [18].

| **RGB Wide Camera** | |
|---|---|
| Sensor | 1/2.3" CMOS, 12 MP |
| Resolution | 4056×3040 |
| Spectral Band | Visible spectrum |
| DFOV | 82.9° |
| Focal Length | 4.5 mm (24 mm eq.) |
| Aperture | f/2.8 |
| **Thermal IR Camera** | |
| Sensor | Uncooled VOx Microbolometer |
| Resolution | 640×512 (16 bit, R-JPEG) |
| Spectral Band | 8–14 $\mu$m |
| DFOV | 40.6° |
| Focal Length | 13.5 mm (58 mm eq.) |
| Aperture | f/1.0 |
| Temperature Range | -40°C–150°C (HG) |

With this set-up, a survey of the facade was conducted. Photogrammetry on vertical structures presents several challenges for path planning, particularly due to the absence of a reference plane for defining parallel trajectories. For this reason, the survey was performed manually by following a zigzag flight pattern at a stand-off distance of 5 m from the building. A total of 1,300 images were captured at 0.5 m intervals to ensure sufficiently high overlap for computing the Structure from Motion (SfM) of the scene. Image acquisition was synchronised, allowing the IR and RGB images to be correlated, and their timestamps were recorded in a .txt file.

### 2.2 Camera Pose estimation

For the camera pose estimation, Agisoft Metashape software is used. First, Ground Control Points (GCPs) are manually annotated within the images, and their corresponding 3D coordinates, measured independently, are input into the software. Using this information, the Structure from Motion (SfM) of the images is computed. The software applies feature extraction algorithms to detect distinctive points in the images, which are then matched and correlated across overlapping photos to compute the 3D camera poses (position and orientation).

All data are expressed in the reference frame of the DISTO X6 rangefinder, whose origin and orientation are defined by the base reference station. To integrate this information within the BIM model, the 3D point cloud derived from Metashape is used to compute the coordinate transformation. First, a coarse registration is performed by aligning corresponding point pairs from the BIM geometry and the point cloud. Reference points, such as corners and window locations, are manually selected in both geometries, and a rigid transformation is computed to align the two datasets. To further improve the registration, the Iterative Closest Point (ICP) algorithm is applied to locally refine the alignment and maximise the overlap between the two geometries. Once these transformations are computed, the camera poses in the BIM reference frame are obtained, as illustrated in Figure 3. Note that the displayed geometry corresponds to the BIM 3D model rather than the photogrammetry point cloud; the point clouds are used solely to align the camera poses within the BIM reference frame.

To verify the reconstruction accuracy, the Root Mean Square Error (RMSE) in the fitting of GCPs was measured in Metashape, yielding a value of 2.8 cm. Overall, all camera poses could be computed with high precision, which minimises projection errors in the IR imagery. As both cameras are mounted in a rigid dual-camera setup, the resulting pixel errors in the IR projections are expected to be on the same order of magnitude, which is highly accurate given the resolution of the thermal imagery. This result was achieved thanks to the precise measurement of GCPs with a laser system and the presence of textured, recognisable patterns on the building facade, which facilitated the SfM calculation.

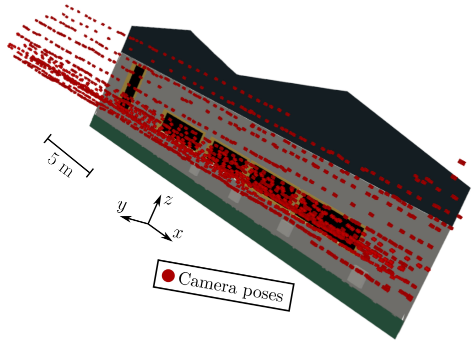


Figure 3. 3D camera-pose estimation using Agisoft Metashape. Red dots indicate the camera poses next to the BIM geometry.

Although this approach requires photogrammetry post-processing, its main advantage is the high accuracy of camera pose estimation, which minimises projection errors in the reconstructed temperature field. Furthermore, because the sensors are synchronised, the pose of the IR camera can be computed automatically from the RGB camera, streamlining the reconstruction workflow.

Alternative approaches, such as LiDAR, do not allow for direct pose calculation because they do not acquire data in a shutter-like manner, which complicates sensor synchronisation. Instead, LiDAR sensors steer infrared beams continuously, recording returns over multiple timestamps during each scan sweep. Another limitation is that the geometric accuracy of LiDAR strongly depends on precise navigation or SLAM systems for point cloud motion correction. To prevent potential drifts that could cause geometric distortions, GNSS RTK systems are typically required. However, these systems are highly susceptible to GNSS signal occlusions and multipath effects, which can be particularly limiting during close-range inspections where accurate positioning is critical. Furthermore, the geometric accuracy of lightweight LiDAR sensors—commonly mounted on UAVs—is generally comparable to, or even lower than, that of photogrammetry, with RMSE values typically on the order of a few centimetres [19].

### 2.3 Thermal field reconstruction

For the thermal field reconstruction, the surface of the BIM model is rasterised at a 3 cm resolution. For each point, denoted as $\mathbf{X}^i_{\text{BIM}}$, the corresponding radiance values from the IR images are extracted using a pinhole camera model. First, the coordinates of each point are expressed in the camera reference frame using Equation (1):

$$\mathbf{X_c}^{i,j} = \begin{bmatrix} X_c^{i,j} \\ Y_c^{i,j} \\ Z_c^{i,j} \end{bmatrix} = \mathbf{R}^j\,\mathbf{X}^i_{\text{BIM}} + \mathbf{t}^j. + \begin{bmatrix} d \\ 0 \\ 0 \end{bmatrix} \tag{1}$$

where:

- $\mathbf{X_c}^{i,j}$ are the coordinates of $\mathbf{X}^i_{\text{BIM}}$ in the reference frame of camera pose $j$.
- $\mathbf{R}^j$ and $\mathbf{t}^j$ are the rotation matrix and translation vector associated with camera pose $j$.
- $d$ is a translation constant equal to 4.5 cm. Note that the camera poses computed in Section 2.2 correspond to the RGB sensor. In the Zenmuse H20T, the IR sensor is aligned with the RGB camera but is spatially separated, as shown in Figure 4.

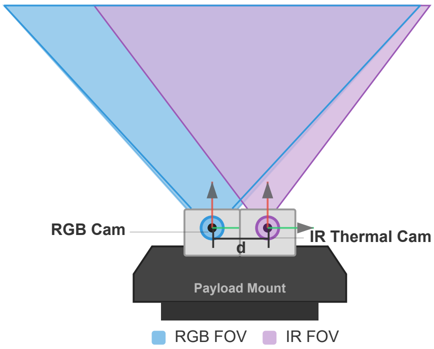


Figure 4. Layout of the Zenmuse H20T. The IR and RGB sensors are aligned along the camera's $x$-axis but are separated by a distance $d$.

The corresponding pixel coordinates $u^{i,j}$ and $v^{i,j}$ are then obtained using Equation (2):

$$u^{i,j} = f\frac{X_c^{i,j}}{Z_c^{i,j}} + c_x, \qquad v^{i,j} = f\frac{Y_c^{i,j}}{Z_c^{i,j}} + c_y, \tag{2}$$

where $f$ is the focal length of the camera in pixel units, and $c_x$ and $c_y$ are the coordinates of the principal point (optical centre) on the image plane. All these quantities are derived from the specifications listed in Table 1.

For each pixel coordinate, the following verifications are performed to ensure projection robustness:

1. **Incidence angle filter.** Using the facade STL mesh derived from the Metashape photogrammetry reconstruction, the surface normal vector $\mathbf{n}$ at each facade point $\mathbf{X}_{\text{STL}}$ is obtained. For each camera position $\mathbf{t}^j$, the viewing direction vector is defined as

$$\mathbf{d} = \mathbf{t}^j - \mathbf{X}_{\text{STL}}. \tag{3}$$

The incidence angle $\theta$ is computed as

$$\cos\theta = \frac{\mathbf{n}\cdot\mathbf{d}}{\|\mathbf{d}\|}. \tag{4}$$

To ensure robustness with respect to normal orientation, the absolute value is considered. A sample is accepted only if

$$|\cos\theta| \geq \cos(\theta_{\min}) = 0.5, \tag{5}$$

which corresponds to a maximum allowable incidence angle of $\theta_{\max} = 60°$. This condition rejects grazing views, which are more sensitive to emissivity effects, ensuring that camera viewing directions are approximately perpendicular to the facade surface.

2. **Visibility / self-occlusion test.** For each valid projection, defined by the direction vector $\mathbf{d}$ and camera pose $\mathbf{t}^j$, a visibility check is performed using the Möller-Trumbore algorithm. Ray-triangle intersection tests are carried out with the STL mesh obtained from the photogrammetric reconstruction, removing projections that fall on occluded regions.

Only the values of $u^{i,j}$ and $v^{i,j}$ that satisfy these conditions are retained, and the corresponding radiance values are extracted from the infrared images. The average radiance at each facade point is then computed. Note that only camera poses for which the point lies within the camera field of view are considered in this calculation.

To obtain absolute temperature fields, reference temperature values are sampled at the facade points shown in Figure 5 using a contact probe Testo 720. The measurements are performed manually by directly recording the in-situ temperature at each point (Figure 6). Thermal paste is applied to ensure good thermal contact with the surface, thereby improving the accuracy of the probe readings. Measured temperatures are correlated with IR camera radiance values at the same locations, and linear regression is used to obtain the absolute temperature fields of the facade surface.

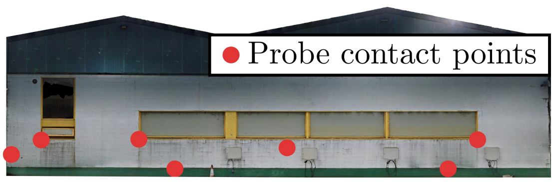


Figure 5. Probe contact point location across the facade surface

Note that this approach assumes uniform thermal emissivity across the facade surface. While this simplification is convenient, it may introduce temperature measurement errors in cases where the facade exhibits significant variations in emissivity, as is typically the case for glass surfaces such as windows. However, since the majority of the surface consists of concrete—with relatively uniform optical properties—and given that the primary focus of the inspection is on this material (as windows provide limited relevant information), a simple linear calibration was deemed appropriate for this case study. Nevertheless, for buildings with more heterogeneous material compositions, the proposed methodology could be extended by incorporating material-specific calibration procedures for different facade elements.

Figure 6. Reference temperature sampling using a Testo 720 probe.

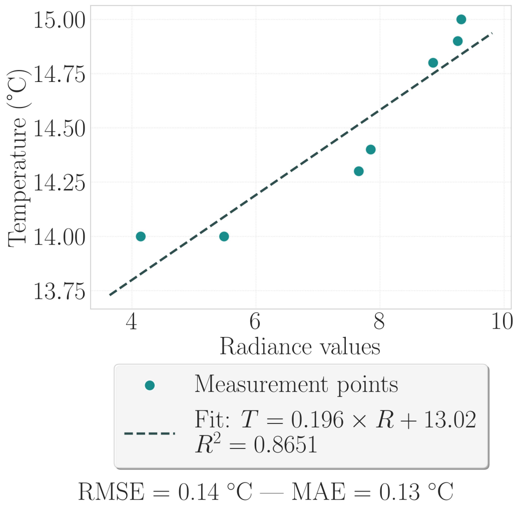


Figure 7. IR camera calibration. A linear regression is employed to correlate radiance values with absolute temperatures measured with the probe.

## 3 Results

Figure 7 shows the results of the IR-camera calibration (Section 2.3), obtained using the absolute temperature values measured by the contact probe. The probe measurements and the average radiance recorded by the IR camera over the rasterised facade surface deviate to some extent from the fitted line. However, this scatter is expected and consistent with typical error sources in IR imagery [20, 21]. Differences in emissivity among facade materials, sensor noise, and temperature variations during the acquisition can fully explain the observed deviations, which are on the order of several tenths of a degree. Nevertheless, the data still exhibits a reasonable linear correlation, with an $R^2$ coefficient of 0.8651. The fitted line indicates that temperature changes only slightly with radiance, with a slope of 0.196 and an intercept of 13.02. A Root Mean Square Error (RMSE) of 0.14ºC between the adjusted line is obtained, a fairly accurate value. These differences can be attributed to several factors, including sensor noise, temperature variations between probe sampling and image acquisition, or measurement errors.

Figure 8 shows the reconstructed temperature field of the facade overlaid with the semantic surface segmentation of the BIM model. Overall, the temperature remains nearly constant across the facade wall, with only minor variations of a couple of degrees near the upper left and right corners. These differences are likely due to measurement errors from the IR camera. In these corners, the camera was pointing in the direction of the sun, and this radiation may have affected the readings.

Although the different facade components are made of materials with varying absorption coefficients, the facade remained in the shade during the inspection and in the preceding hours of the morning, which explains the observed uniformity in the temperature field.

For the integration of inspection data within standardised BIM formats such as IFC, the semantically segmented facade components are mapped to BIM-native entities, creating a structured, object-based representation of the building envelope. In this framework, thermographic analysis can be used to detect potential deficiencies, such as localised thermal anomalies, which are then associated with the corresponding BIM elements. When identified, these deficiencies can be incorporated as property sets linked to the affected objects, optionally including their spatial coordinates. This enriched, object-level representation enables the integration of inspection results into a unified BIM model, supporting condition assessment and maintenance workflows while ensuring interoperability.

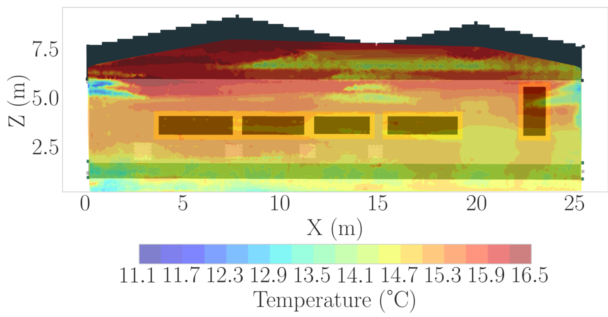


Figure 8. Overlay of the facade temperature field on the components of the BIM model.

Figure 9 displays a histogram of the temperature distribution across the raster points of the facade. As shown, most points remain at a temperature of around 15 °C, with only a few outliers reaching values as low as 12 °C. However, the frequency of these outliers is minimal and, as discussed previously, they can likely be attributed to IR measurement errors. Overall, the temperature field remains uniform, and no insulation deficiencies or moisture accumulation issues are observed.

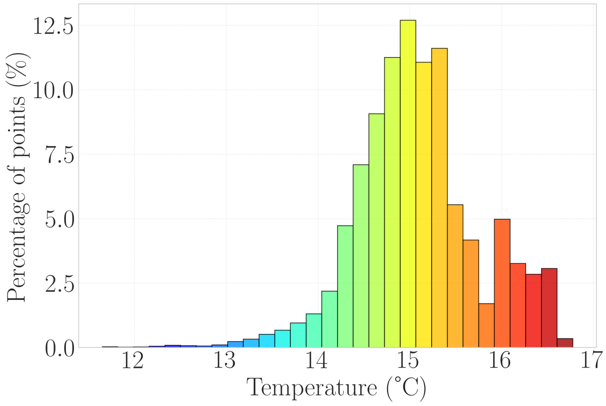


Figure 9. Histogram of the facade temperature distribution.

To verify the consistency of the results, the reconstructed temperature field is compared with the air temperature at the time of the inspection. Table 2 shows the air temperature during the inspection, retrieved from a nearby meteorological station managed by MeteoGalicia in Ourense [22], the region's main meteorological agency. The station is situated within the University of Vigo campus, at a distance of approximately 1 km from the inspected building facade. As shown, the air temperature remained within 15–16 ºC during the inspection, which is consistent with the measured temperature field.

Table 2. Temperature measurements from MeteoGalicia's station on 06/11/2025 [22].

| Time | Temperature (°C) |
|---|---|
| 12:00:00 | 14.92 |
| 12:10:00 | 15.00 |
| 12:20:00 | 15.20 |
| 12:30:00 | 16.20 |
| 12:40:00 | 16.66 |
| 12:50:00 | 15.86 |
| 13:00:00 | 15.62 |

Figure 10 shows the number of viewing cameras at each point of the projected raster model. As observed, the distribution of viewing cameras is not uniform, since the facade inspection was conducted by manually piloting the UAV. To improve inspection uniformity, automatic path planning tools could be employed. In general, however, almost all raster points exhibit a high camera count. During the facade survey, a total of 1,433 images of the wall were captured (Figure 3), resulting in a high level of overlap between photographs.

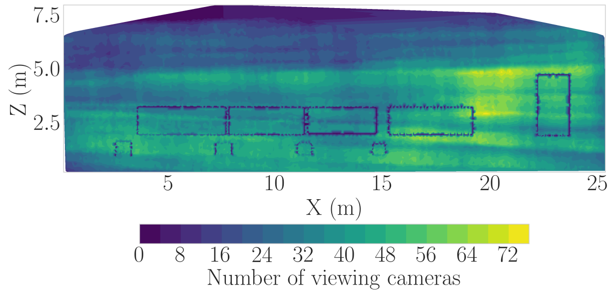


Figure 10. 2D map of the number of cameras viewing the facade surface.

Figure 11 presents a histogram of the distribution of viewing cameras. Most points are observed by 10 or more cameras, with an average of 36.76 viewpoints across the facade surface. Only in isolated cases does the camera count fall below 10, primarily at points near the building roof where fewer images of the facade were acquired. This highlights one of the main advantages of UAV imagery over traditional methods: up to thousands of images of the entire facade can be captured in just a few minutes, significantly reducing both inspection time and the associated operational risk.

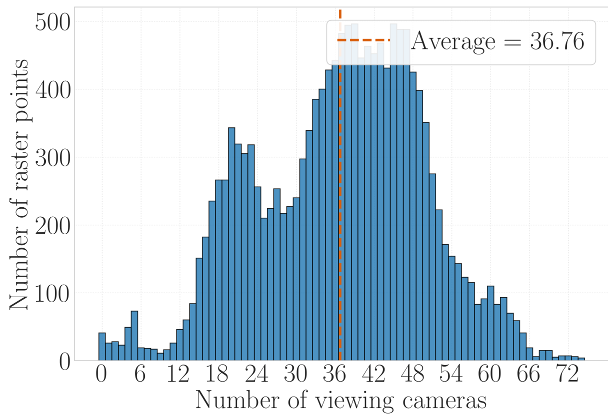


Figure 11. Histogram of the number of cameras viewing the facade.

## 4 Conclusions

This work presents an automated workflow for the efficient reconstruction of facade temperature fields using UAVs. Visual imagery is used to perform Structure-from-Motion and estimate camera poses, and this information is then employed to project IR radiance fields onto a BIM model of the structure. Absolute temperature values are obtained through a radiometric calibration using contact probes. To validate the proposed approach, a case study was conducted in Ourense, where a temperature field of the facade was reconstructed and segmented according to the BIM model surfaces. Overall, a uniform temperature field was observed, as the inspected wall was in the shade. The results were also consistent with the air temperature values recorded at a nearby meteorological station, further supporting the validity of the method.

In future work, the methodology will be integrated with path planning and autonomous navigation systems to enable more efficient and fully automated facade inspections. Additionally, artificial intelligence algorithms will be incorporated for automatic defect detection, and the approach will be validated on facades exhibiting moisture, thermal bridges, and insulation deficiencies to quantify the accuracy of the proposed pipeline. Inspections of facades under sunlight exposure will also be conducted to assess the impact of solar radiation on the measured temperature values and the accuracy of insulation defect detection, thereby further validating the methodology under varied environmental conditions.

## Acknowledgements

This work was funded by the European Union - Horizon Europe, Agencia Estatal de Investigación, Ministerio de Ciencia, Innovación y Universidades, and Xunta de Galicia through the following grants: SARIL A302, STORCITO 101182153, RADIANCE 101235536, PID2021-125060OB-I00 A202, PID2024-156356OB-I00 A507, CPP2022-009679 A308, FPU21/01176, FEADER2024/052B A406, Ciencias Mariñas-MRR C286, GPC-ED431B 2025/31 A505.

## References

[1] Elton Bauer, Elier Pavón, Eva Barreira, and Eliane Kraus De Castro. Analysis of building facade defects using infrared thermography: Laboratory studies. *Journal of Building Engineering*, 6, 2016. ISSN 23527102. doi:10.1016/j.jobe.2016.02.012.

[2] Jun Chen, Shenghan Zhang, Gang Zhao, Dhanada Mishra, and Matthew Ming Fai Yuen. Infrared thermography of façade delamination: Quantifying environmental variability and heat transfer mechanisms. *Construction and Building Materials*, 494, 2025. ISSN 09500618. doi:10.1016/j.conbuildmat.2025.143177.

[3] Ali Waqas, Mohamad T. Araji, and Sherif S. Sherif. A novel method for monitoring material behaviour in urban buildings using aerial multi-modality imaging. *Building and Environment*, 282, 2025. ISSN 03601323. doi:10.1016/j.buildenv.2025.113300.

[4] Marta Videras Rodríguez, Sergio Gómez Melgar, and José Manuel Andújar Márquez. Evaluation of aerial thermography for measuring the thermal transmittance (U-value) of a building façade. *Energy and Buildings*, 324, 2024. ISSN 03787788. doi:10.1016/j.enbuild.2024.114874.

[5] Yinglong He, Jiayu Pan, Ramit Debnath, Ronita Bardhan, Luke Cullen, Marco Gomez Jenkins, Erik Mackie, George Hawker, and Ian Parry. Energy mapping of existing building stock in cambridge using energy performance certificates and thermal infrared imagery. *Environmental Data Science*, 3, 2025. ISSN 26344602. doi:10.1017/eds.2024.26.

[6] Alberto Villarino, Hugo Valenzuela, Natividad Antón, Manuel Domínguez, and Ximena Celia Méndez Cubillos. Uav applications for monitoring and management of civil infrastructures. *Infrastructures*, 10(5), 2025. doi:10.3390/infrastructures10050106.

[7] Mariluz Gil-Docampo, Juan Ortiz Sanz, Ignacio Cañas Guerrero, and Manés Fernández Cabanas. Uas ir-thermograms processing and photogrammetry of thermal images for the inspection of building envelopes. *Applied Sciences*, 13(6):3948, 2023.

[8] Albert Ficapal and Ivan Mutis. Framework for the detection, diagnosis, and evaluation of thermal bridges using infrared thermography and unmanned aerial vehicles. *Buildings*, 9, 2019. ISSN 20755309. doi:10.3390/buildings9080179.

[9] Tarek Rakha and Alice Gorodetsky. Review of Unmanned Aerial System (UAS) applications in the built environment: Towards automated building inspection procedures using drones. *Automation in Construction*, 93:252–264, 2018. ISSN 0926-5805. doi:10.1016/j.autcon.2018.05.002.

[10] Adam Dlesk, Karel Vach, and Karel Pavelka. Transformations in the Photogrammetric Co-Processing of Thermal Infrared Images and RGB Images. *Sensors*, 21(15), 2021. doi:10.3390/s21155061.

[11] Yingying Kong, Henry Leung, Bowen Zhang, Shiyu Xing, and Yingying Chen. 3-D Point Cloud Reconstruction of Infrared Images Based on Improved Structure from Motion. In *2018 2nd European Conference on Electrical Engineering and Computer Science (EECS)*, pages 307–310, 2018. doi:10.1109/EECS.2018.00063.

[12] Krishna Ribeiro-Gomes, David Hernández-López, José F. Ortega, Rocío Ballesteros, Tomás Poblete, and Miguel A. Moreno. Uncooled Thermal Camera Calibration and Optimization of the Photogrammetry Process for UAV Applications in Agriculture. *Sensors*, 17(10), 2017. doi:10.3390/s17102173.

[13] Adam Dlesk, Karel Vach, and Karel Pavelka. Photogrammetric Co-Processing of Thermal Infrared Images and RGB Images. *Sensors*, 22(4), 2022. doi:10.3390/s22041655.

[14] Rudraksh Kapil, Guillermo Castilla, Seyed Mojtaba Marvasti-Zadeh, Devin Goodsman, Nadir Erbilgin, and Nilanjan Ray. Orthomosaicking Thermal Drone Images of Forests via Simultaneously Acquired RGB Images. *Remote Sensing*, 15(10), 2023. doi:10.3390/rs15102653.

[15] Agisoft LLC. Agisoft metashape. `https://www.agisoft.com/`, 2025.

[16] Pix4D. Pix4dmapper. `https://www.pix4d.com/`, 2025.

[17] Leica Geosystems. Leica disto x6 laser distance meter. Product page, 2025. URL `https://shop.leica-geosystems.com/global/measurement-tools/disto/leica-disto-x6/buy`. Accessed: 2025-12-11.

[18] DJI. Zenmuse h20 series specifications. `https://enterprise.dji.com/zenmuse-h20-series/specs`, 2025. Accessed: 2025-12-11.

[19] J. D. D. Casisirano and A. R. C. Claridades. Comparative analysis of uav photogrammetry and terrestrial laser scanning for 3d building reconstruction. *ISPRS Annals of the Photogrammetry, Remote Sensing and Spatial Information Sciences*, X-5/W4-2025:143–150, 2026. doi:10.5194/isprs-annals-X-5-W4-2025-143-2026. URL `https://isprs-annals.copernicus.org/articles/X-5-W4-2025/143/2026/`.

[20] MG Acorsi, LM Gimenez, and M Martello. Assessing the performance of a low-cost thermal camera in proximal and aerial conditions. remote sens 12: 3591, 2020.

[21] Krishna Ribeiro-Gomes, David Hernández-López, José F Ortega, Rocío Ballesteros, Tomás Poblete, and Miguel A Moreno. Uncooled thermal camera calibration and optimization of the photogrammetry process for uav applications in agriculture. *Sensors*, 17(10):2173, 2017.

[22] MeteoGalicia. MeteoVisor: observación meteorolóxica en Galicia. `https://www.meteogalicia.gal/web/observacion/meteovisor`, 2025. Accessed: 2025-12-11.